Microstructural Analysis of Fusion Zone in Gas Tungsten Arc-Welded Newly Developed Co-Based Superalloy

H.R. ABEDI and O.A. OJO

The fusion zone (FZ) microstructure of a newly developed gas tungsten arc-welded cobalt-based superalloy called CoWAlloy1 is characterized. Elemental microsegregation leads to the formation of interdendritic micro-constituents, which are confirmed to include MC-type carbides and γ-γ' eutectics, as well as inhomogeneous precipitation of γ' within the FZ. The presence of the terminal solidification reaction products and inhomogeneous distribution of γ' in the FZ require appropriate consideration during the development of optimal post-weld heat treatment.

https://doi.org/10.1007/s11661-021-06541-w

THE development of γ' ($Co_3(Al,W)$) precipitation-strengthened cobalt (Co)-based superalloys as first reported by Sato *et al.*[1] has recently attracted increasing interest due to their superior high-temperature mechanical properties.[2] Among these novel superalloys, CoWAlloy1 is a newly developed γ' ($Co_3(Al,W)$) precipitation-strengthened Co-based superalloy that has been replacing conventional nickel (Ni)-based superalloys for elevated-temperature applications that exceed 750 °C.[3] This alloy has the unique characteristics of a high volume fraction of the γ' phase (50 pct),[4] low creep rate,[3] large processing temperature window (235 °C),[4] and high oxidation resistance,[3] and therefore surpasses the performance of some of the conventional Ni-based superalloys such as Waspaloy, Udimet 720Li, and IN738. Welding superalloys is an essential task in the manufacture and repair of complex-shaped components of gas turbine engines. Among the various welding processes, gas tungsten arc welding (GTAW) has been extensively used for welding superalloys in the fusion welding process.[5] The mechanical properties of these weldments greatly depend on the microstructural changes of the weld. Lampman[6] reported that non-equilibrium solidification during the GTAW process leads to dendritic microsegregation in the fusion zone (FZ). Dendritic microsegregation typically causes the formation of solidification constituents within the interdendritic region and the inhomogeneous distribution of secondary phase precipitates. These microstructural changes are known to considerably affect the properties of the FZ.[4]

Ding *et al.*[7] reported that the formation of non-equilibrium eutectic-type micro-constituents can reduce the resistance to hot cracking in the FZ. Brooks and Krenzer[8] showed that FZ cracking in the A-286 superalloy is attributed to the presence of a low-melting Laves phase in the FZ. Similarly, Ding *et al.*[7] who investigated a Ni_3Al-based alloy, IC6, showed that the formation of nickel–molybdenum (NiMo; Y) and γ–γ' eutectic phases leads to severe FZ cracking. Osoba *et al.*[9] reported that the high cracking resistance of the FZ in Haynes 282 could be due to the inhibition of the formation of a deleterious γ–γ' eutectic.[9] Ojo *et al.*[10] concluded that the formation of low-melting solidification constituents such as M_3B_2 and Ni_7Zr_2 in the FZ of IN738LC increases susceptibility to cracking in the post-weld heat treatment (PWHT).

Furthermore, in some instances, the elements that form the main strengthening phase could be combined with the subsequent non-equilibrium intermetallic precipitates, which leads to the inhomogeneous distribution of the γ' strengthening phase. This can have detrimental effects on the mechanical properties at elevated temperatures.[10,11] Ojo *et al.*[10] also confirmed the formation of non-homogeneously distributed γ' particles in the FZ of IN738LC. They showed that the FZ microstructure consists of coarse γ' precipitates in the interdendritic regions and fine γ' precipitates in the dendrite core. Similarly, Chen *et al.*[12] observed the non-uniform distribution of the γ' precipitates in iron–nickel (Fe–Ni)-based alloy following post-weld aging treatment. They concluded that this inhomogeneity results in reduced microhardness of the FZ compared to the base metal with a uniform distribution of γ' particles.[12]

H.R. ABEDI and O.A. OJO are with the Department of Mechanical Engineering, University of Manitoba, Winnipeg, R3T 5V6 Canada. Contact e-mail: abedineh@myumanitoba.ca; olanrewaju.ojo@umanitoba.ca

Manuscript submitted August 13, 2021; accepted November 5, 2021.

Article published online December 2, 2021

The detrimental microstructural changes in the FZ summarized above can be remedied through PWHT to modify the as-welded microstructure and release the residual stresses. Strum *et al.*[11] reported that the as-weld microstructures are the primary factors that determine how superalloy welds respond to PWHT. There are limited studies on the weldability of γ' ($Co_3(Al,W)$) precipitation-strengthened Co-based superalloys,[2] and there is no reported study that focused on the FZ microstructure of CoWAlloy1. Therefore, this work aims to investigate the FZ microstructure of gas tungsten arc-welded CoWAlloy1, which will ultimately contribute to the development of an appropriate PWHT process that would enhance the properties of the material after welding.

CoWAlloy1 was in the form of cast produced using vacuum induction melting process, followed by hot isostatic pressing (HIP) at 1200 ºC and 15 ksi for 4 hours to remove the porosities and also to homogenize the microstructure. The polycrystalline CoWAlloy1 has a chemical composition of 30.6 pct Ni, 10.2 pct chromium (Cr), 2.6 pct aluminum (Al), 9.0 pct tungsten (W), 4.4 pct tantalum (Ta), 2.0 pct titanium (Ti), 0.3 pct hafnium (Hf), 0.2 pct silicon (Si), 0.02 pct carbon (C), 0.01 pct boron (B), and 0.02 pct zirconium (Zr), and a balanced wt pct of Co. The welding coupon was wire cut by using an electric discharge machine (EDM) into dimensions of 75 × 20 × 5 mm. The welding input parameters used in the GTAW process are listed in Table I. Subsequently, the welded sample was sectioned transversely to the weld. The specimens were mounted and grounded with 600 SiC and 1200 SiC sand papers, followed by polishing with a 6- and 1-μm diamond suspension, respectively. To reveal the dendritic microstructure of the FZ, the specimens were chemically etched with a solution of 50 mL of hydrochloric acid + 50 mL of distilled water + 10 g of copper sulfate. In addition, the specimens were electrochemically etched with a solution of 96 mL of sulfuric acid + 80 mL of nitric acid + 24 mL of phosphoric acid for 3 seconds at 5 V to examine the details of the FZ microstructure. The initial microstructural investigation was conducted by using a Zeiss Axiovert 25 optical microscope. Further microstructural characterization was carried out with a JEOL-5900LV scanning electron microscope and FEI Talos F200X transmission electron microscope. The two microscopes were used with Oxford energy-dispersive spectrometer. The sample that was subjected to transmission electron microscopy (TEM) was prepared by grinding the sample into 3-mm-diameter foils with a thickness of 120 μm. Subsequently, the foils were electro-polished in a solution of 900 mL methanol + 100 mL perchloric acid at – 30 ºC and 1 V. Furthermore, the composition of the dendrite core regions within the FZ was quantitatively determined by using a CAMECA SX100 electron microprobe analyzer (EPMA).

Table I. Welding Parameters of the GTAW Process

Parameter	
Voltage (V)	10
Current (A)	60
Velocity (mm/min)	50
Shielding gas flow rate (l/h)	60

Figure 1 shows an optical micrograph of the FZ with a cellular–dendritic microstructure. The secondary dendrite arm spacing (SDAS) ranges from 6 to 10.4 μm, and the average value is calculated to be 8.2 μm.

Generally, the SDAS is known to have a direct relationship with the cooling rate as follows[12]:

$$\lambda_s = a\theta^{-n}, \quad [1]$$

where λ_s represents the SDAS, a and n are constants and governed by the alloy structure, and θ is the cooling rate. The values of $a = 50$ μm and $n = 0.3$ were taken from Norman *et al.*[13] to evaluate the cooling rate from the calculated SDAS. Osoba *et al.*[9] reported that the degree of solid-state diffusion throughout the solidification process is mainly governed by the cooling rate. The cooling rate in the FZ was calculated to be around 414 °C/s. The average chemical composition of 20 points in the center of the dendrite cores near the FZ boundaries was evaluated by using the EPMA and the values are summarized in Table II. From these data, the partition coefficient of the solute elements, which represents the degree and direction of microsegregation throughout the solidification process, was calculated by simplifying the solute redistribution model developed in Bower *et al.*[14] In this study, a rapid cooling rate is assumed to significantly limit the degree of solute back-diffusion. Another implicit assumption is that throughout the solidification process, the solute elements are not significantly diffused throughout the solid. Therefore, by neglecting undercooling at the dendrite edges, the solute redistribution at the beginning of solidification can be described reasonably well by using

$$k = \frac{C_s}{C_0}, \quad [2]$$

where C_s and C_0 are the element compositions in the dendrite core and nominal composition, respectively, and k denotes the equilibrium partition coefficient.

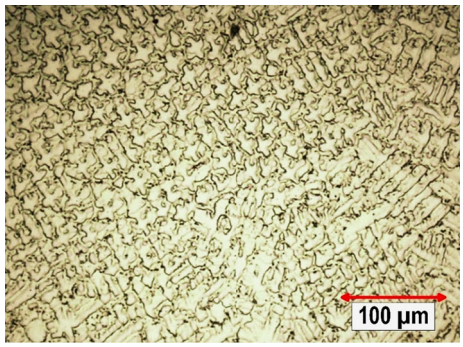

Fig. 1—Optical micrograph of the FZ.

Table II. Chemical Composition (Weight Percent) of Dendrite Core and Calculated Partition Coefficient (K)

Element	Co	Ni	Cr	Al	W	Ti	Ta	Si	Hf	Zr
Dendritic Core (Wt pct)	41.72	29.56	11.18	2.34	9.71	1.44	3.43	0.012	0.057	0.006
$K = C_s/C_o$	1.02	0.97	1.09	0.88	1.08	0.74	0.77	0.68	0.19	0.42

Table II provides the initial partition coefficients of the alloying elements at the beginning of the solidification process. The result shows that Co and Ni have K values near unity, thus indicating that these elements segregate fairly uniformly between the dendrite core and interdendritic regions. In contrast, W and Cr have $K > 1$, which shows that they segregate to the dendrite regions, while Al, Ta, Ti, Hf, Si, and Zr have $K < 1$, which shows they partition to the interdendritic region. The observed microsegregation behavior of the elements is in good agreement with the findings of the previous research on Co-based superalloys.[15–20] The partition coefficients of B and C could not be evaluated because of difficulties in obtaining accurate quantification for these two light elements, and the impact of their back-diffusion can be substantial throughout the solidification process. Liu *et al.*[2] showed that the partition coefficient of C in Co–Al–W-based superalloys is less than unity and segregates into the interdendritic liquid during solidification. Similarly, Sun *et al.*[21] showed that the partition coefficient of B in a Co-based superalloy, DZ40M, is less than unity, and partitions to the interdendritic regions. Therefore, in the current work, it is reasonable to infer that during the weld solidification of CoWAlloy1, both B and C mainly segregate to the interdendritic regions. Ojo *et al.*[10] also reported that even though the partition coefficients are not necessarily constant throughout the solidification process, they can be well adapted to explain the formation of interdendritic micro-constituents.

Figure 2 shows a SEM image of a typical FZ microstructure. It can be seen that the interdendritic areas contain isolated second phase particles that have blocky and rod-like morphologies (Particles A) and micro-constituents with a crown-like morphology (micro-constituent B). Initial X-ray energy-dispersive spectroscopy (EDS) analysis on the interdendritic particles A, using the SEM, indicated that the particles are rich in MC-type carbide-forming elements such as Ta, Hf, and Ti. The SEM did not reveal the presence of γ' precipitates in the FZ. In order to positively identify the interdendritic particles A and micro-constituents B, TEM analyses were performed. Figure 3(a) shows the bright-field TEM image of particle A. TEM–EDS microanalysis on particle A listed in Table III reveals that this particle is rich in MC-type carbide-forming elements of Ta, Ti, and Hf. An analysis of the selected area diffraction pattern (SADP) obtained from various zone axes (Figures 3(b) to (d)) indicates that the phase is MC-type carbide with a face-centered cubic (FCC) crystal structure and lattice parameter of 4.32 Å. In addition to the MC-type carbides, TEM analysis shows that the micro-constituents B are γ–γ' eutectics, as

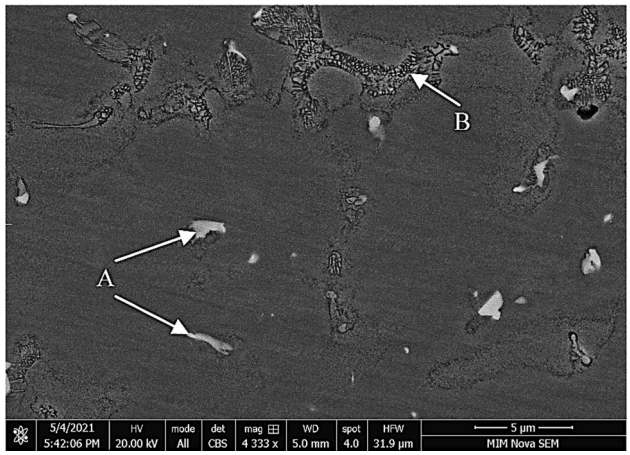

Fig. 2—SEM micrograph of the FZ.

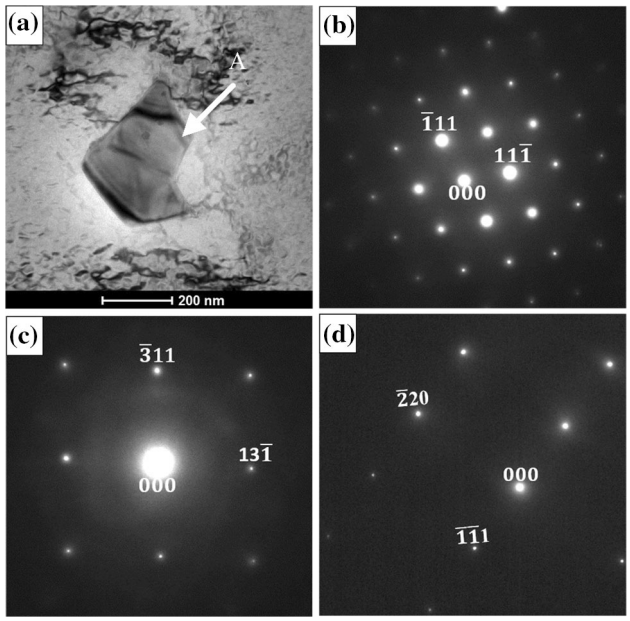

Fig. 3—TEM examination on particle A. (*a*) Bright-field TEM image of the block-shaped particle A and SADP of particle A from zone axes of (*b*) [101], (*c*) [215], and (*d*) [112].

confirmed through SADP obtained from the [112] zone axis (inset of Figure 4). Furthermore, aside from the γ–γ' eutectics, γ' precipitates are also observed through the dark-field TEM imaging technique (Figure 4) to have formed within the FZ. However, the size of the γ' precipitates varies with location, such that regions close to the γ–γ' eutectics are observed to have coarser γ'

Table III. Semi-Quantitative TEM/EDS Microanalysis of Particle A

Element	Co	Ni	Cr	W	Ti	Ta	Hf	Zr
(Wt Pct)	2.10	1.51	1.14	4.93	20.77	53.05	14.97	1.47

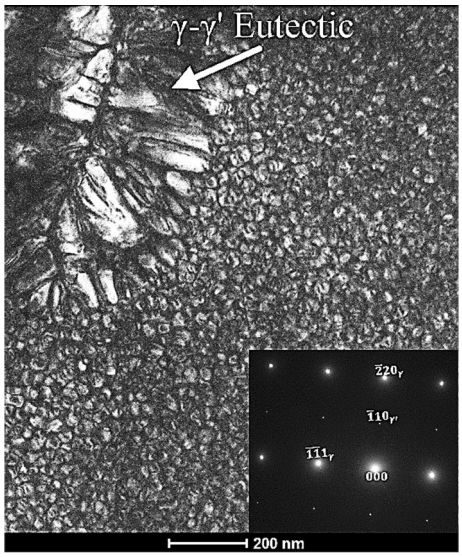

Fig. 4—Dark-field TEM image showing the presence of γ–γ' eutectics and γ' precipitates with non-uniform distribution in the interdendritic region and inset SADP obtained from the [112] zone axis.

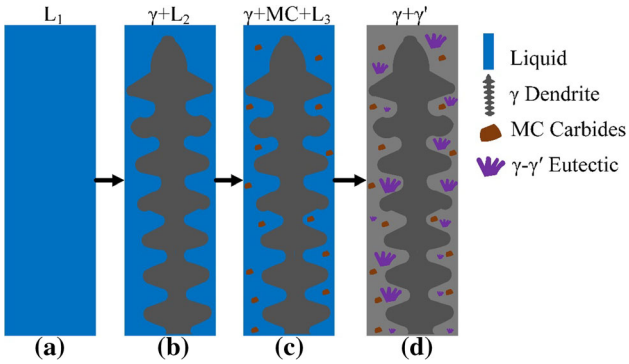

Fig. 5—Schematic of the solidification reaction product sequence in CoWAlloy1 showing the formation of (*a*) Liquid (L_1), (*b*) γ Dendrite through a $L_1 \rightarrow \gamma + L_2$ reaction, (*c*) MC-type carbide through a $L_2 \rightarrow \gamma + MC + L_3$ reaction. (*d*) γ–γ' Eutectic through a $L_3 \rightarrow \gamma + \gamma'$ eutectic-type reaction.

precipitates compared to regions further away from the eutectics (Figure 4).

The microstructural evolution in the FZ is generally governed by two solidification processes: dendrite formation and solute distribution. To study the solidification behavior in CoWAlloy1, JMatPro (7.0.0 version), a thermodynamics-based software, was used. Solidification reaction products were computed based on the Scheil–Gulliver solidification model. Several studies have reported that the Scheil–Gulliver solidification model can accurately predict the solidification behavior of superalloys.[22–25] Figure 5 shows the schematic of the solidification reaction product sequence in CoWAlloy1. The solidification process is initiated with the formation of γ dendrites as the primary solid to form out from the liquid through a $L_1 \rightarrow \gamma + L_2$ reaction (Figure 5(b)). As the γ dendrites gradually form and grow, elements with a partition coefficient less than unity are increased in the interdendritic liquid. As the solute rejection of the interdendritic liquid continues during cooling, the solubility limit of the γ dendrites will be exceeded. Thus, secondary solidification constituents form in the interdendritic region. In CoWAlloy1, the carbide-forming elements such as Ti, Ta, Hf, and C show considerable segregation to the interdendritic region. Also, these elements show limited solubility in Co, which results in the formation of MC-type carbides within the interdendritic region through a $L_2 \rightarrow \gamma + MC + L_3$ reaction over a range of temperatures (Figure 5(c)). As cooling continues, the supersaturation of the residual interdendritic liquid with γ' forming elements such as Al, Ti, and Ta would occur and eventually lead to the formation of γ–γ' eutectics through a $L_3 \rightarrow \gamma + \gamma'$ eutectic-type reaction over a range of temperatures (Figure 5(d)). Zhou *et al.* examined the solidification path of novel γ/γ' in Co-based superalloys and reported that γ–γ' eutectics form at the terminal stage of solidification.[17]

Further cooling to a temperature that is adequately lower than the γ' solvus temperature of 1070 °C[3] would cause the formation of γ' precipitates to commence. The segregation of γ' forming elements during solidification can lead to the formation of γ' precipitates in the interdendritic regions at higher temperatures. The higher Al and Ti contents in the interdendritic region are known to increase the γ' solvus temperature.[26,27] Therefore, as more time is available for the γ' precipitates to grow in the interdendritic region, this can lead to the formation of coarser γ' precipitates in the interdendritic regions, as observed in the present work. The non-uniform distribution of γ' particles can, however, deteriorate the high-temperature properties and is one of the main reasons that necessitate the use of PWHT of superalloy weldments.

Cracking in superalloys is known to be the primary defect that can occur during PWHT. Several probable reasons for the PWHT cracking in superalloys have been previously discussed in Thamburaj *et al.*[28] In the currently studied material, incipient melting of γ–γ' eutectics either during the heating stage of multipass welds or during the solutionizing heat treatment of PWHT could increase susceptibility to FZ cracking. Consequently, the presence of terminal solidification products in CoWAlloy1, as found in the present work, is an essential factor that requires attention during the

development of the PWHT process to enhance the properties of the superalloy after welding.

The microsegregation behavior observed throughout the solidification of CoWAlloy1 with GTAW indicates that Co and Ni segregate fairly uniformly between the dendrites and interdendritic regions. On the other hand, W and Cr somewhat segregate to the dendrites, while Al, Ta, Ti, Hf, Si, and Zr tend to partition to the interdendritic liquid. This elemental microsegregation leads to the formation of secondary solidification products consisting of MC-type carbides and γ–γ' eutectics within the interdendritic regions. Furthermore, TEM analysis reveals the inhomogeneous distribution of γ' precipitates within the FZ. The formation of low-melting terminal solidification reaction product, γ–γ' eutectics, and non-homogeneously distributed γ' precipitates within the FZ require adequate consideration in the development of an optimum PWHT process for homogenizing and improving mechanical properties of the CoWAlloy1 superalloy.

The authors would like to acknowledge the Natural Sciences and Engineering Research Council of Canada and the University of Manitoba for providing financial support.

The authors declare that they have no known competing financial interests or personal relationships that could have appeared to influence the work reported in this paper.

REFERENCES

1. J. Sato, T. Omori, K. Oikawa, I. Ohnuma, R. Kainuma, and K. Ishida: *Science*, 2006, vol. 312, pp. 90–91.
2. C. Liu, Y. Sun, M. Wen, T. He, and J. Yu: *J. Manuf. Process.*, 2020, vol. 56, pp. 820–29.
3. S. Neumeier, L.P. Freund, and M. Göken: *Scr. Mater.*, 2015, vol. 109, pp. 104–07.
4. L.P. Freund, S. Giese, D. Schwimmer, H.W. Höppel, S. Neumeier, and M. Göken: *J. Mater. Res.*, 2017, vol. 32, pp. 4475–82.
5. J. Chen, E. Salvati, F. Uzun, C. Papadaki, Z. Wang, J. Everaerts, and A.M. Korsunsky: *J. Manuf. Process.*, 2020, vol. 53, pp. 190–200.
6. S. Lampman: *Weld Integrity and Performance*, ASM International, New York, 1997.
7. R.G. Ding, O.A. Ojo, and M.C. Chaturvedi: *Scr. Mater.*, 2006, vol. 54, pp. 859–64.
8. J.A. Brooks and R.W. Krenzer: *Weld. J. (Miami, Fla).*, 1974, vol. 53, pp. 4–7.
9. L.O. Osoba, R.G. Ding, and O.A. Ojo: *Mater. Charact.*, 2012, vol. 65, pp. 93–99.
10. O.A. Ojo, N.L. Richards, and M.C. Chaturvedi: *Scr. Mater.*, 2004, vol. 51, pp. 683–88.
11. M.J. Strum, L.T. Summers, and J.W. Morris: *Weld. J.*, 1983, vol. 62, pp. 235s–242s.
12. S. Chen, H. Hu, M. Zhao, and L. Rong: *Mater. Sci. Eng. A*, 2018, vol. 718, pp. 363–70.
13. A.F. Norman, R. Ducharme, A. Mackwood, P. Kapadia, and P.B. Prangnell: *Sci. Technol. Weld. Join.*, 1998, vol. 3, pp. 260–66.
14. T.F. Bower, H.D. Brody, and M.C. Flemings: *Trans. Metall. Soc. AIME*, 1966, vol. 236, pp. 624–33.
15. J. Koßmann, C.H. Zenk, I. Lopez-Galilea, S. Neumeier, A. Kostka, S. Huth, W. Theisen, M. Göken, R. Drautz, and T. Hammerschmidt: *J. Mater. Sci.*, 2015, vol. 50, pp. 6329–38.
16. S.P. Murray, K.M. Pusch, A.T. Polonsky, C.J. Torbet, G.G.E. Seward, N. Zhou, S.A.J. Forsik, P. Nandwana, M.M. Kirka, R.R. Dehoff, W.E. Slye, and T.M. Pollock: *Nat. Commun.*, 2020, vol. 11, pp. 1–11.
17. X. Zhou, H. Fu, Y. Zhang, H. Xu, and J. Xie: *Adv. Eng. Mater.*, 2019, vol. 21, pp. 1–10.
18. C.A. Stewart, S.P. Murray, A. Suzuki, T.M. Pollock, and C.G. Levi: *Mater. Des.*, 2020, vol. 189, p. 108445.
19. X. Zhou, H. Fu, Y. Zhang, H. Xu, and J. Xie: *J. Alloys Compd.*, 2018, vol. 768, pp. 464–75.
20. M. Tsunekane, A. Suzuki, and T.M. Pollock: *Intermetallics*, 2011, vol. 19, pp. 636–43.
21. Z. Sun, X. Chen, L. Zhang, S. Zhang, and J. Feng: *Curr. Comput.-Aided Drug Des.*, 2021, https://doi.org/10.3390/cryst11050479.
22. N. Saunders, A.P. Miodownik, and J.P. Schillé: *J. Mater. Sci.*, 2004, vol. 39, pp. 7237–43.
23. J. Kangazian, M. Shamanian, A. Kermanpur, E. Foroozmehr, and M. Badrossamay: *Mater. Sci. Eng. A*, 2021, vol. 823, p. 141742.
24. A. Ghasemi, A.M. Kolagar, and M. Pouranvari: *Mater. Sci. Eng. A*, 2020, vol. 793, p. 139861.
25. P. Tao, H. Li, B. Huang, Q. Hu, S. Gong, and Q. Xu: *Vacuum*, 2019, vol. 159, pp. 382–90.
26. M. Ooshima, K. Tanaka, N.L. Okamoto, K. Kishida, and H. Inui: *J. Alloys Compd.*, 2010, vol. 508, pp. 71–78.
27. Y. Zhang, H. Fu, X. Zhou, Y. Zhang, and J. Xie: *Mater. Sci. Eng. A*, 2018, vol. 737, pp. 265–73.
28. R. Thamburaj, W. Wallace, and J.A. Goldak: *Int. Met. Rev.*, 1983, vol. 28, pp. 1–22.